# CM² MAGAZINE

第 26 期

南方科技大学海洋磁学中心主编

# 创刊词

海洋是生命的摇篮，是文明的纽带。地球上最早的生命诞生于海洋，海洋里的生命最终进化成了人类，人类的文化融合又通过海洋得以实现。人因海而兴。

人类对海洋的探索从未停止。从远古时代美丽的神话传说，到麦哲伦的全球航行，再到现代对大洋的科学钻探计划，海洋逐渐从人类敬畏崇拜幻想的精神寄托演变成可以开发利用与科学研究的客观存在。其中，上个世纪与太空探索同步发展的大洋科学钻探计划将人类对海洋的认知推向了崭新的纬度：深海（deep sea）与深时（deep time）。大洋钻探计划让人类知道，奔流不息的大海之下，埋藏的却是亿万年的地球历史。它们记录了地球板块的运动，从而使板块构造学说得到证实；它们记录了地球环境的演变，从而让古海洋学方兴未艾。

在探索海洋的悠久历史中，从大航海时代的导航，到大洋钻探计划中不可或缺的磁性地层学，磁学发挥了不可替代的作用。这不是偶然，因为从微观到宏观，磁性是最基本的物理属性之一，可以说，万物皆有磁性。基于课题组的学科背景和对海洋的理解，我们对海洋的探索以磁学为主要手段，海洋磁学中心因此而生。

海洋磁学中心，简称 $CM^2$，一为其全名“Centre for Marine Magnetism”的缩写，另者恰与爱因斯坦著名的质能方程 $E = MC^2$ 对称，借以表达我们对科学巨匠的敬仰和对科学的不懈追求。

然而科学从来不是单打独斗的产物。我们以磁学为研究海洋的主攻利器，但绝不仅限于磁学。凡与磁学相关的领域均是我们关注的重点。为了跟踪反映国内外地球科学特别是与磁学有关的地球科学领域的最新研究进展，海洋磁学中心特地主办 $CM^2$ Magazine，以期与各位地球科学工作者相互交流学习、合作共进！

“海洋孕育了生命，联通了世界，促进了发展”。 21 世纪是海洋科学的时代，由陆向海，让我们携手迈进中国海洋科学的黄金时代

# 目 录

# 第 16 章　MD 颗粒的热剩磁（TRM）与地磁场古强度

SD 颗粒的热剩磁符合尼尔理论，具有完美的独立性、可逆性和可叠加性。而 MD 颗粒 M 的变化是由磁畴壁移动造成的，这种行为就比较复杂。比如对 SD 颗粒来说，在（$T_1$，$T_2$）温度区间获得的 pTRM（$T_1$，$T_2$），只能在（$T_1$，$T_2$）区间解阻，被热退磁。但是，这个规则对 MD 颗粒不成立。

我们来做一个实验，类似于 SD 颗粒，我们也让 MD 颗粒获得一个（$T_1$，$T_2$）温度区间的 pTRM（$T_1$，$T_2$），然后对这个剩磁进行热退磁。结果发现，在 $T_1$ 之前，pTRM 就已经开始部分解阻了；到了 $T_2$ 的时候，还有一小部分剩磁没有退完，需要更高的温度才能把它完全退磁。这到底是什么原因呢？

MD 颗粒的剩磁是由于磁畴壁移动造成的。磁畴壁移动的路径上会存有很多沟沟坎坎。只要一加热，磁畴壁就会克服一些小的沟坎，向原始的平衡状态转化，所以在 $T_1$ 之前就会被部分退磁。到达了 $T_2$ 时，还有一些更高的沟坎没有被克服，也就是会遗留一小部分剩磁。

我们把 $T_1$ 之前退掉的剩磁叫做 pTRM“前尾巴”，把 $T_2$ 之上才退掉的剩磁叫做后尾巴。这些尾巴会对 Arai-plot 造成什么样的影响呢？

因为有了前尾巴，MD 颗粒的 TRM 在低温段会更容易退磁，在 Arai-plot 上面，点会向下移动。在 $T_2$ 之上，因为存在后尾巴，TRM 相对不容易被退磁。这两种情况叠加起来，就会形成一种向下凹陷的曲线。

面对这种曲线，我们就会显得很棘手。到底用那一段去拟合直线，进而计算斜率呢？显然，在低温段，斜率会偏大，估算的古强度会偏高。那么用高温段的

数据拟合直线，斜率会偏低。总之，对 MD 颗粒而言，用哪一个温度段的数据去拟合直线都无法得到准确的地磁场古强度。

自然样品中，PSD/MD 颗粒是最为常见的磁畴状态，常常和 SD 颗粒混在一起。既然 MD 颗粒会造成 Arai-plot 行为扭曲，我们能不能在实验过程中把 MD 颗粒的影响去除掉?

那我们就来分析一下 SD 和 MD 颗粒的磁学行为到底有什么不同。SD 颗粒非常稳定，其矫顽力一般大于 20 mT。而 MD 颗粒的剩磁不稳定，其矫顽力一般要小于 20 mT。

有了这个物理基础，我们就可以利用二者之间矫顽力的不同来加以区分。最为有效的就是交变场（Alternating field，AF）退磁。

AF 退磁过程需要用到交变场。目前实验室的 AF 最大峰值一般可到 100-150 mT，最高可到 300 mT。在实验过程中，设定一个峰值 AF 和衰变频率（decay rate），在零场中，让 AF 场逐渐衰减到零。我们可以想象，变化磁场，其实就是让外场克服 $H_k$，从而让 M 达到相对混乱地排列的效果。

对于 MD 颗粒，将 AF 峰值设定为 20 mT 就可以有效地去除其携带的剩磁。所以，在传统的 Thellier 地磁场古强度实验中，在每一步之前我们都进行 20 mT AF 退磁，就有可能压抑 MD 颗粒的剩磁影响，从而突出 SD 的剩磁行为。

对于 MD 颗粒，除了 AF 退磁，还有一种退磁方式叫做低温旋回（Low-T cycling，LTC）退磁。其基本原理是，磁畴壁对高温和低温都敏感。在低于 300 K，随着降温，磁畴会发生变化。但是当回到 300 K 时，却不能返回到初始状态，于是就达到了部分退磁的目的。想实现 LTC 退磁，还是很容易的。在零磁环境里，把古地磁样品泡到液氮里，然后捞出来升到室温，就实现了 LTC 退磁。

无论是 AF 退磁，还是 LTC 退磁，都大大地增加实验步骤，使得古强度实验变得非常繁琐，让人望而却步。

如果你认为这样就可以获得完美的古强度数据了，那就太小看这个研究方向了。影响实验结果的因素非常多，我们接下来娓娓道来。

之前我们说过，即使对 SD 颗粒，它的磁化需要时间。如果降温速度太快，SD 颗粒可能就没有时间被充分磁化，其 TRM 就会低一些。反之，如果降温很慢，SD 颗粒就能被充分磁化，达到最佳磁化状态，TRM 就会高。所以，降温速率确实会影响 TRM 的强度，当然也会影响对 $H_0$ 的估算。

对于一组具有单轴各向异性的 SD 颗粒，其获得的热剩磁与饱和等温剩磁的比值为：

$$M_{TRM}/M_{rs} = 2\ln(f_0 t)H/H_K(T_B)$$

受到降温速率的影响。Stacey 和 Banerjee (1974)推导出

$$T = [kT_B/\Delta E(T_B)][T_B/(-dT/dt)]$$

其中$\Delta E$是能垒。

联合这两个式子可以看出，TRM 的获得与降温速率反相关。降温越慢，TRM 越大。

自然界中，熔岩流的降温可能需要几个月甚至更长的时间，而实验室获得 TRM 的过程降温只需要一两个小时，所以降温速率相差好几个数量级。于是，我们必须要做降温速率补偿。

如果存在明显的各向异性，我们还需要进行 AMS 校正。除了火山岩，考古陶片或者砖头都可以被用来研究地磁场古强度。不过这些人工烧制的东西，压实度很大，AMS 也就很大，会对剩磁状态产生影响。

古地磁强度试验，需要反复加热，造成矿物转化。为了减小这种加热影响，John Shaw 教授提出了一种新方法，只需要一步加热获得完全的 TRM 即可。为了矫正加热前后可能的矿物转化的影响，会测量样品加热前后的非磁滞剩磁（anhysteretic remanent magnetization，ARM，我们之后会讲到这个剩磁），$ARM_1$ 和 $ARM_2$。同时这两个 ARM 的比值还可以用来作为校正系数。我们把这种测量方法称之为 Shaw 方法。

为了确保实验结果可靠，大家还常常同时做 Thellier 和 Shaw 方法。如果两种方法的结果很一致，就加大了数据结果的可靠性。可是，即使是 Shaw 方法，也需要加热，就难免还是要产生氧化等影响。于是，又有科学家从加热炉子入手，往炉子里通入氩气，这样在加热过程中，就不会发生氧化，从而确保了样品的新鲜度。

# 文献导读

## 1. 循环的古老地壳熔融导致了古登堡不连续面的形成

**翻译人：冯婉仪 fengwy@sustech.edu.cn**

*Liu J, Hirano N, Machida S, et al.* ***Melting of recycled ancient crust responsible for the Gutenberg discontinuity****[J].* ***Nature communication****, 2020, 11: 172.*

**摘要：**在岩石圈-软流圈边界的地震速度不连续面被称为古登堡不连续面，它的成因仍是一个谜。虽然人们经常认为地幔部分熔融形成的熔体可以解释这种不连续现象，但目前还不清楚是哪些因素决定性地控制了熔体的产生。在这里，我们报道的地球化学证据表明，在岩石圈-软流圈边界的熔体分数的增加不仅是由与循环的古老海相沉积物有关的碳酸盐熔体堆积导致的，而且与循环的大洋榴辉岩/辉石岩有关的富集辉石岩地幔的部分熔融密切相关。这一结论是根据存在明确的古登堡不连续面的西北太平洋板块上喷发的一套年轻的 petit-spot 玄武岩的 Mg 同位素数据得出来的。我们的研究结果揭示了在正常大洋之下的古登堡不连续面与在地球深部循环的古老俯冲地壳和碳酸盐之间的特殊联系。

**ABSTRACT:** A discontinuity in the seismic velocity associated with the lithosphere-asthenosphere interface, known as the Gutenberg discontinuity, is enigmatic in its origin. While partial mantle melts are frequently suggested to explain this discontinuity, it is not well known which factors critically regulate the melt production. Here, we report geochemical evidence showing that the melt fractions in the lithosphere-asthenosphere boundary were enhanced not only by accumulation of compacted carbonated melts related to recycled ancient marine sediments, but also by partial melting of a pyroxene-rich mantle domain related to the recycled oceanic eclogite/pyroxenites. This conclusion is derived from the first set of Mg isotope data for a suite of young petit-spot basalts erupted on the northwest Pacific plate, where a clearly defined Gutenberg discontinuity exists. Our results reveal a specific linkage between the Gutenberg discontinuity beneath the normal oceanic regions and the recycling of ancient subducted crust and carbonate through the deep Earth.

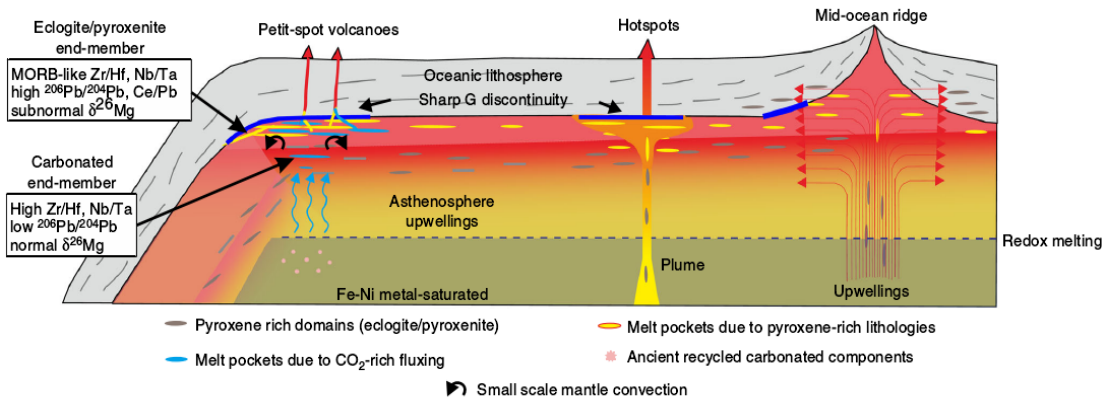


Figure 1. Schematic cross-section of the oceanic mantle illustrating potential mechanisms that could concentrate partial melts below the oceanic LAB. The G discontinuity (bold dark blue lines) corresponds to the melt layer enhanced by the stagnation of partial melt at the base of the lithosphere. The dark gray lenses show pyroxene-rich heterogeneities due to recycling of ancient crustal materials. They will develop melt pockets in the shallow LVZ (yellow lenses) due to different scale of upwelling of the asthenosphere at ridges, hotspots or near the subduction zone4, and stretched horizontally due to the mantle flow[11]. Beneath the old oceanic lithosphere where petit-spot basalts erupted, two end-members of recycled components (recycled carbonated marine sediments and the recycled oceanic eclogite/pyroxenite) contribute to the formation of partial melts that finally generate melt layers beneath the LAB and cause the origin of the G discontinuity. See the text for the details of the model.

## 2. 地磁场强度变化在核幔边界的磁通量喷出的痕迹

**翻译人：李园洁 liyj3@sustech.edu.cn**

*Troyano M, Fournier A, Gallet Y, et al.* ***Imprint of magnetic flux expulsion at the core-mantle boundary on geomagnetic field intensity variations[J]. Geophysical Journal International****, 2020, 221(3): 1984-2009.*

**摘要**：过去的十几年，近东和西欧的考古地磁数据发现，地磁场强度的快速或极端变化与高于当前观测到的最大值频率有关。最极端的事件称为地磁 spikes，定义为在短时间内（几十年）内发生的强度突增，其特征是变化率高，最高可达每年数 μT。一些学者认为来自地球外核的磁通量喷发，可能解释这些峰值，但尚未进行详细研究。本文，我们建立了一个二维的磁通量喷出运动学模型，其关键控制参数是磁雷诺数 Rm，即磁扩散时间与平流时间之比。该模型能够跟踪磁力线，其由于一个固定的流动模式而发生变形和折叠。控制系统的磁场演化有两个过程。第一个是从封闭的流线中产生磁通量，从而磁通量逐渐集中在区域的边界附近，这使得系统的磁能增加。如果上边界将导电流体与绝缘介质分开，则会发生第二个过程，即通过该界面的扩散过程，我们可以通过监控沿该边界的磁感应垂直分量的演化来量化该过程。正是这两个过程的结合，决定了通过核-幔边界的磁通量喷出模型。我们分析几种具有不同流动模式和磁边界条件的参数配置。我们首先关注单个涡流的通量排出。由于已经对该配置已经进行了广泛的研究，因此我们将其成功用于将我们的分析解决方案以及以前发布的数值结果进行基准测试。接下来，我们将注意力转向一种配置，涉及两个反向旋转的涡流，这些涡流在畴的中心产生上升流，并包括与绝缘介质的上边界。我们发现逃离畴尺度的磁场垂直分量的特征上升时间和最大瞬时变化率分别约为 和 。将这些缩放定律推算到地球范围上可与近东和西欧报道的的各种据称的考古地磁强度高值进行了比较。根据我们的数值实验，磁通量排出不太可能产生地磁峰值，而更长的持续时间（一个世纪或更长时间）和较小的变化率的强度峰值似乎与此过程相关。

**ABSTRACT:** During the last decade, rapid or extreme geomagnetic field intensity variations associated with rates greater than the maximum currently observed have been inferred from archeomagnetic data in the Near-East and in Western Europe. The most extreme events, termed geomagnetic spikes, are defined as intensity peaks occurring over a short time (a few decades), and are characterized by high variation rates, up to several μT/yr. Magnetic flux expulsion from the Earth's outer core has been suggested as one possible explanation for these peaks but has not yet been examined in detail. In this study, we develop a two dimensional kinematic model for magnetic flux expulsion whose key control parameter is the magnetic Reynolds number Rm, the ratio of magnetic diffusion time to advection time. This model enables the tracking of magnetic field lines which are distorted and folded by a fixed flow pattern. Two processes govern the magnetic evolution of the system. The first one is the expulsion of magnetic flux from closed streamlines, whereby flux

gradually concentrates near the boundaries of the domain, which leads to an increase of the magnetic energy of the system. If the upper boundary separates the conducting fluid from an insulating medium, the second process takes place, that of diffusion through this interface, which we can quantify by monitoring the evolution of the vertical component of magnetic induction along this boundary. It is the conjunction of these two processes that defines our model of magnetic flux expulsion through the core-mantle boundary. We analyse several configurations with varying flow patterns and magnetic boundary conditions. We first focus on flux expulsion from a single eddy. Since this specific configuration has been widely studied, we use it to benchmark successfully our implementation against analytic solutions and previously published numerical results. We next turn our attention to a configuration which involves two counter-rotating eddies producing an upwelling at the center of the domain, and comprises an upper boundary with an insulating medium. We find that the characteristic rise time and maximum instantaneous variation rate of the vertical component of the magnetic field that escapes the domain scale like and , respectively. Extrapolation of these scaling laws to the Earth's regime is compared with various purported archeointensity highs reported in the Near-East and in Western Europe. According to our numerical experiments magnetic flux expulsion is unlikely to produce geomagnetic spikes, while intensity peaks of longer duration (one century and more) and smaller variation rates appear to be compatible with this process.

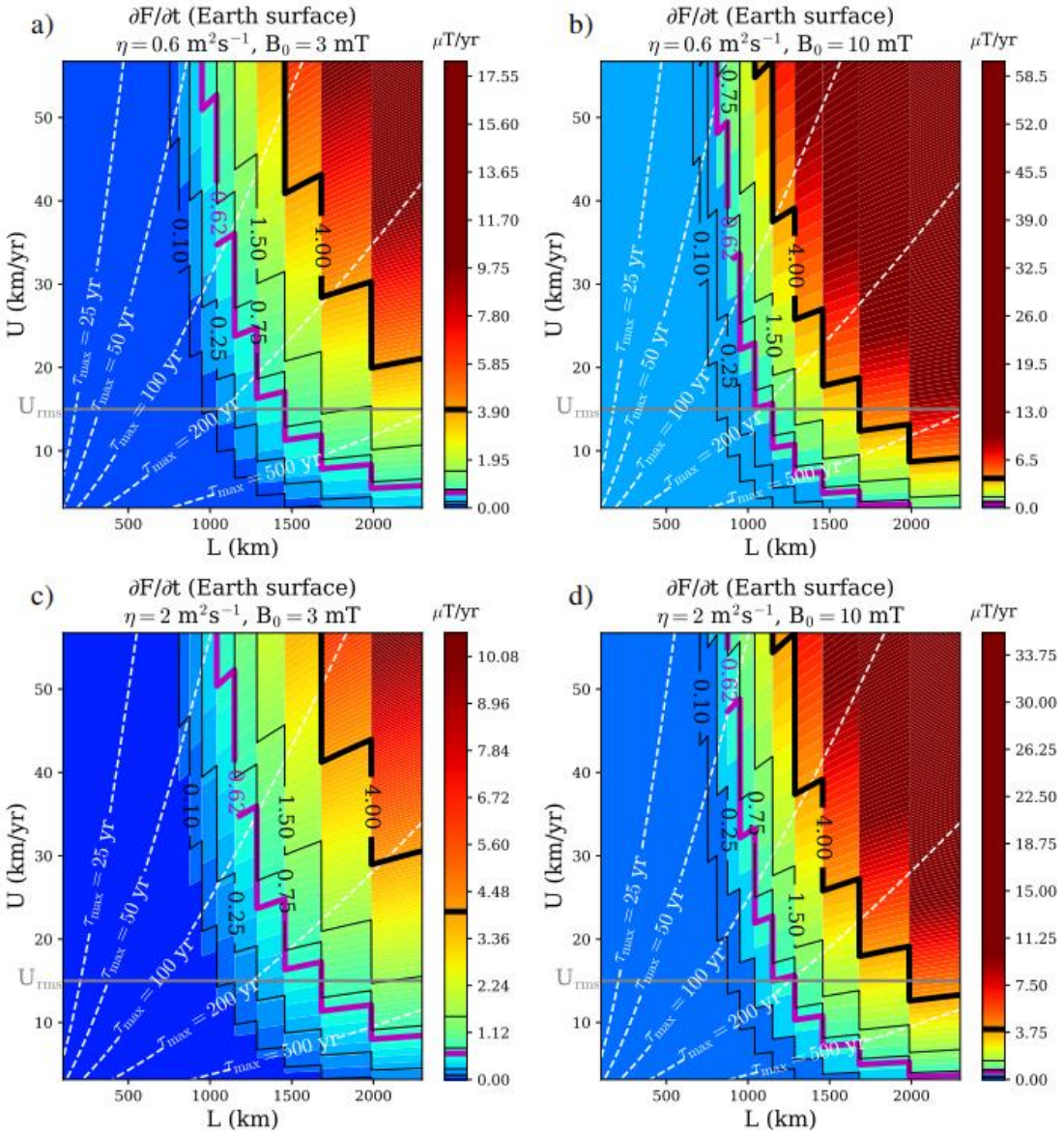


Figure 1. Instantaneous rate of change of the intensity of the field generated by flux expulsion as a function of the characteristic velocity of the fluid in the Earth's core and the characteristic scale of the process in the core, given for different initial intensity and magnetic diffusivity. Urms is the root mean square velocity at the top of the core. The solid lines represent some constant rates of change. The dashed lines give different values of τmax corresponding to half of the total duration of the expected peak of intensity induced by flux expulsion at the CMB.

## 3. 冰消期深海 Si 的重新运移指示冰期生物地球化学和物理作用控制的大气二氧化碳水平

翻译人：蒋晓东 jiangxd@sustech.edu.cn

*Pichevin, L. E., Ganeshram, R. S., Dumont, M. (2020).* ***Deglacial Si remobilisation from the deep-ocean reveals biogeochemical and physical controls on glacial atmospheric $CO_2$ levels****. Earth and Planetary Science Letters.543, 116332*

**摘要：**在末次冰期，缓慢的深海循环将碳封存到深渊中导致大气中二氧化碳的降低。这种生物代谢至关重要的营养盐受影响而重新分布，然而相关的理解仍不充分。末次冰消期东太平洋赤道区域硅藻的硅同位素 $\delta^{30}Si$ 和生物堆积速率，为我们提供了溶解态硅和碳从大洋底部重新运移的证据。因为在海表溶解态硅对硅藻的生长至关重要，它的浓度在冰期的深海区对海洋二氧化碳摄取是负反馈。然而，这一影响可以被增强的铁输入缓和，因为在贫铁海域它（如东太平洋赤道区域）降低了硅藻对硅的需求。结果表明在冰期间冰期转换期间，生物二氧化碳泵的效率和本地二氧化碳来源的多少均受溶解态硅利用率变化的强烈控制，而可利用铁的量驱动该控制过程。

使用调整后的潘多拉盒模型揭示，全球大洋表层海水溶解态硅的存量受控于高盐低叶绿素区铁的可利用率而不是上升流直接供应的硅。全新世的特点是在贫铁和有效翻转的条件下生物对硅的高需求导致了硅的快速循环，通过快速耗尽表面的溶解态硅促进二氧化碳排放和生物碳泵低效化。末次冰期锯齿使海洋硅循环减慢，在海表富铁条件下引起生物所需溶解态硅含量降低，增强了深海硅和二氧化碳的封存。发生在 15 ka 和中冰消期硅循环两个模式的转变，引起生物碳缩减在东太平洋赤道区和全球初度的响应，该响应在冰消期二氧化碳上升的两个模式间进行比较。结果表明，除了深海二氧化碳储存和底流翻转外，生物泵的效率在决定海洋-大气二氧化碳交换中扮演了重要角色，并且揭示海洋循环和可利用铁-硅在这个过程中的双重控制。

**ABSTRACT：**During the last glacial period, the sluggish deep Ocean circulation sequestered carbon into the abyss leading to the lowering of atmospheric $CO_2$. The impact of this redistribution on biologically essential nutrients remains poorly constrained. Using sedimentary $\delta^{30}Si$ of diatoms and biogenic accumulation rates in the Eastern Equatorial Pacific (EEP), we present evidences for the remobilisation of dissolved Silica (DSi) along with carbon from the deep ocean during the Last Deglaciation. Because DSi is essential for diatoms growing in the surface ocean, its concentration

in the abyss during the glacial periods amounts to a negative feedback on the oceanic $CO_2$ uptake. However, this effect can be muted by the increased Fe inputs during glacial periods which reduces diatom Si requirements in Fe limited regions such as the EEP. Our results from the EEP suggest that the efficiency of the biological $CO_2$ pump and the size of the local $CO_2$ source is tightly controlled by changes in DSi utilisation driven by Fe availability across the last glacial-interglacial transition.

We use a modified PANDORA box model to illustrate that the inventory of DSi in the global ocean surface is controlled by Fe availability in HNLC areas rather than by straightforward Si supply though upwelling. The Holocene is characterised by a fast mode of Si cycling driven by high biological requirement for Si under conditions of iron limitation and efficient overturning, promoting $CO_2$ outgassing and an inefficient biological C pump via the rapid exhaustion of DSi in the surface. The last glacial period saw slower marine Si cycling as a result of decreased DSi biological requirement under Fe-replete conditions in the sea surface and increased Si and $CO_2$ sequestration in the abyssal ocean. The switch between the two modes of Si cycling happened at 15 ka BP, i.e. mid-deglaciation, and resulted in contrasting biological carbon drawdown responses in the EEP and globally between both phases of the deglacial $CO_2$ rise. This illustrates that in addition to deep-sea $CO_2$ storage and overturning, the efficiency of the biological pump also plays a crucial role in determining ocean-atmosphere $CO_2$ exchange and shows the dual controls of ocean circulation and Fe-Si availability in this process.

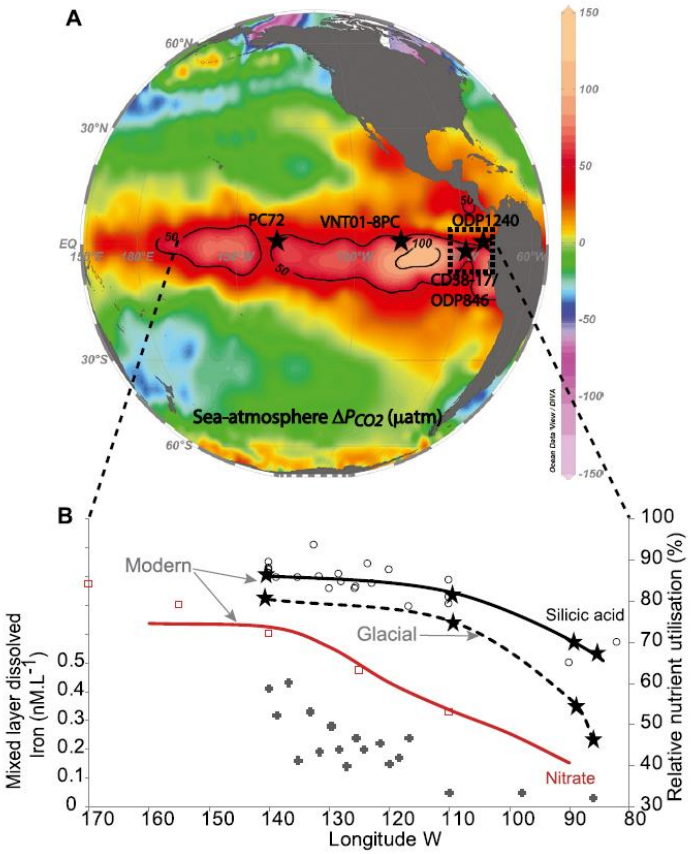


Figure 1. (A) Map of modern sea-atmosphere _$PCO_2$ (µatm) showing the eastern equatorial pacicif (EEP) $CO_2$ source hot spot. Stars mark the core locations (ODP 1240, ODP 846, VNTR01-8PC and PC72) and the box shows the area where the 6 sedimentary archives used to build the export production stack records were retrieved. (B) Silicic acid relative utilisation reconstructed from sea water samples (black circle) and core tops (solid black line, modern time) and glacial age sediment (doted lines) compared with Nitrate relative utilisation from sea water samples (red squares Rafter and Sigman (2016)) and sediment core tops (red line, modern) and with dissolved Fe concentration in the mixed layer (black cross) (Kaupp et al., 2011; Ahlgren et al., 2014). The relative utilisation is calculated using the Rayleigh fractionationation model from N and Si isotopic signals obtained in both core top and sea-surface water samples. Both data sets are in good agreement (see Sup. Mat.). (For interpretation of the colours in the figure(s), the reader is referred to the web version of this article.) Warming and reduction in herbivory increase GPP and ecosystem $CO_2$ uptake potential. Left hand and middle panels show the variation in daytime $CO_2$ fluxes: a, b net ecosystem exchange NEE800, d, e gross primary production GPP800, and g, h ecosystem respiration Re in warmed (red) and ambient (blue) field plots of Subarctic mountain birch forest field layer vegetation (supplemented with cloned birch plantlets) during growing seasons 2017 and 2018 (dots are estimated marginal means ± s.e.m. produced by the fitted statistical model in Table 2; n =5 field plots). Right hand panels show seasonal means ± s.e.m. of c NEE800, f GPP800, and i Re (means are estimated marginal means produced by the fitted statistical model in Table 2, n = 5 field plots examined over 5 [year 2017] or 12 [year 2018] repeated measures). Light tone dashed lines, symbols, and bars denote plots, where herbivory was reduced using an insecticide. The pale yellow background stripe stands for the period of severe hydrological stress (2nd July–1st August, 2018; see Fig. 3). Source data are provided as a Source Data file.

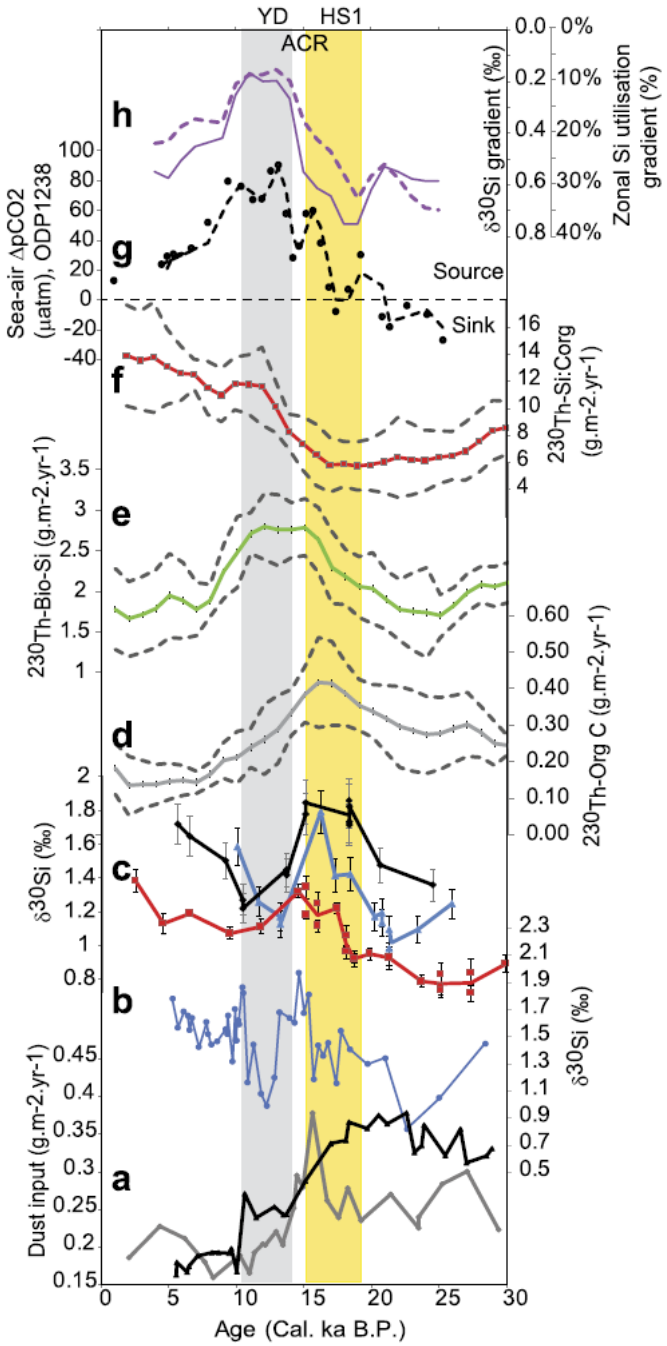


Figure 2. (a) Th232 based dust input from core PC72 (black Winckler et al. (2008)) and ODP1240 (grey); (b) Silicon isotope records from cores MD-773 (Dumont et al., 2020) in the Antarctic; (c) Silicon isotope records from cores ODP 1240 (red), ODP 846 (blue) and VNTR01-8PC (black); Stack records and standard deviation lines (dashed grey lines) of 230Th normalised organic carbon (solid grey, d), biogenic opal (green, e) and Si to Organic carbon accumulation ratio (red, f) in the EEP (core location in table, Sup. Mat. 2); (g) Boron isotope based reconstruction of Sea-air $CO_2$ efflux in the EEP (black dots Martinez-Boti et al. (2015)); and (h) zonal gradients of d30Si (solid purple) and Si relative utilisation (dashed purple, %). YD stands for Younger Dryas, HS1 for Heinrich stadial 1 and ACR for Antarctic Cold Reversal.

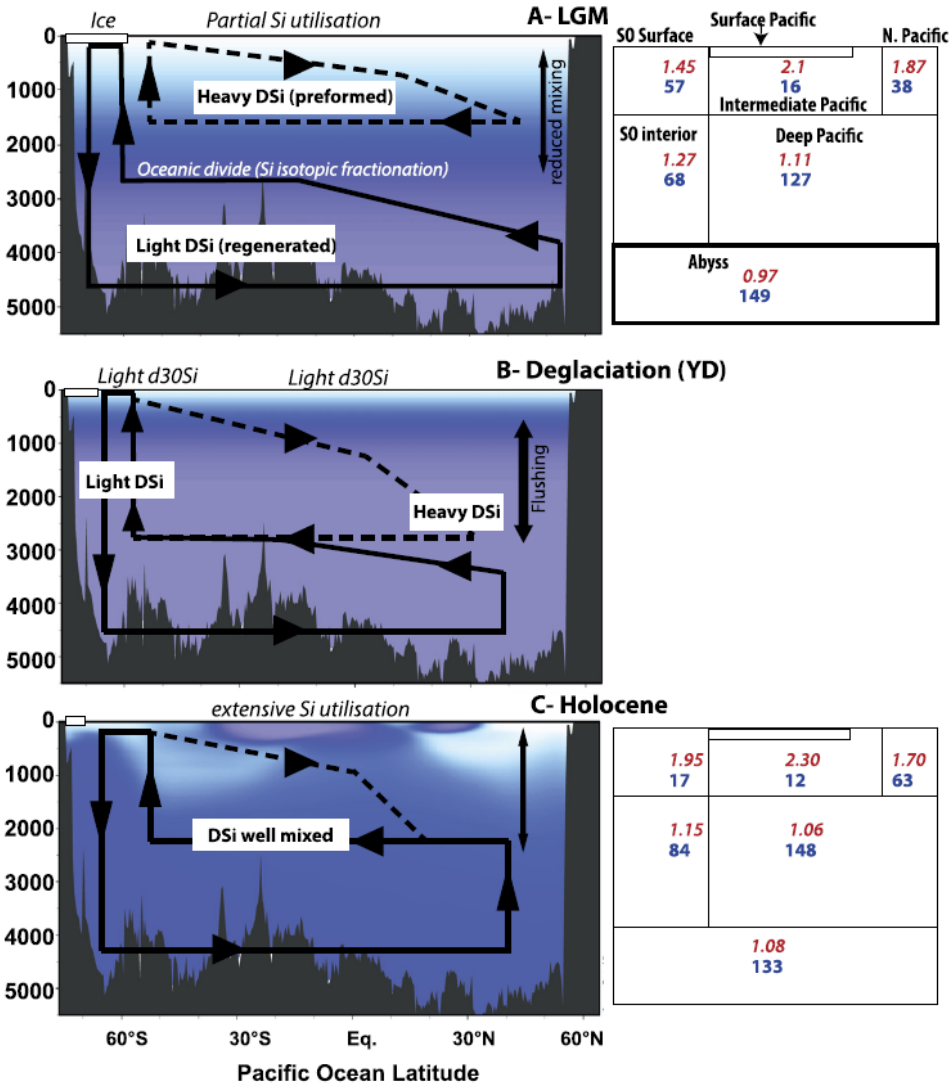


Figure 3. Conceptual model of LGM to Holocene change in Si cycling (left) and the PANDORA simulation of the Pacific and Southern Ocean (SO) for the Last Glacial maximum (LGM) and the Modern (right). A- LGM: The lower and intermediate circulation limbs were separated allowing isotopic segregation between an accumulating stock of regenerated Si (light) at depth and lessening stock of preformed Si (heavy) in the upper circulation branch while Fe replete conditions at the sea surface prevented complete Si utilisation, maintained relatively light $\delta^{30}Si$ in the surface and isotopic fractionation between the regenerated and preformed Si pools. B- Younger Dryas (YD): The deglacial flushing of the regenerated, isotopically light Si pool through the SO after 15 Ka resulted in light Si isotopic signature recorded in the surface of the SO and EEP, whilst the merging between the lower and upper limbs of the ocean circulation (Rae et al., 2018) caused the mixing of the 2 Si pools and the progressive disappearance of the isotopic partitioning. The lower dust inputs caused Fe limitation leading to the establishment of HNLC status in the EEP C- Holocene: DSi overconsumption in HNLC region, Si is exported below the mixed layer and either recirculated or exported at depth, resulting in moderate isotopic partitioning between the surface and the well-mixed ocean interior. The PANDORA box model results illustrate the potential associated changes in DSi concentration (blue, μM.L−1) and isotopic signature (red, ) in Pacific water masses between the LGM and modern conditions. Only the model results for the Pacific and SO are shown (for full model results see Sup. Mat. 3).

## 4. 苏拉威西西南地区石笋在过去 530 ka 中磨损和生长速率的变化

**翻译人：杨会会 11849590@mail.sustech.edu.cn**

*N Scroxton, M K Gagan, G B Dunbar et al.* ***Natural attrition and growth frequency variations of stalagmites in southwest Sulawesi over the past 530,000 years [J].Palaeogeography, Palaeoclimatology, Palaeoecology*** *(2015), doi:10.1016/j.palaeo.2015.10.030*

**摘要**：先前的研究分析了从多个洞穴采集的石笋的年龄分布，并推断了重要的古气候变化，从而解释了石笋的生长阶段。然而，石笋的生长可能跨越了数万年；因此，它们是不可替代的（不可再生的）。石笋对科学研究的价值必须与其潜在的和目前的审美和文化价值进行权衡。在本研究中，我们表明，在不移除石笋的情况下，也可以从洞穴系统中提取一些古气候信息。我们的案例研究在对 77 根石笋的每一根都进行 U-Th 定年的基础上开展的，这些石笋是从印尼苏拉威西岛西南部的 Bantimurung-Bulusaraung 国家公园周围的 13 个洞穴中采集的。在最近的大约 53 万年中，石笋在不同的时间间隔段增长，对其年龄分布的分析显示，从古到今的石笋数量呈一阶指数递减。此外，这种指数关系在世界各地的石笋总数中都可以观察到，因此这很可能是一种普遍的洞穴现象。苏拉威西西南地区的一阶指数年龄分布在 425-400、385-370、345-335、330-315、160-155 ka, 75-70 ka 和 10-5 ka 处的石笋生长频率正异常，这通常与婆罗洲典型的的湿润期一致。为了解释这种分布，我们提出了一个简单的石笋生长和磨损模型。喀斯特系统固有的过程控制着一级趋势，而这些过程控制着石笋的自然磨损。这些过程在时间上几乎是恒定的，导致石笋基底年龄呈指数关系。二阶变化是由气候变化引起的石笋生成速率的变化控制的，这是洞穴文献中一个众所周知的概念。去除指数基线可以更好地评估相对峰值高度，并可以推断出基本的古气候信息。重要的是，一阶和二阶生长频率的变化可以只用石笋基底的年龄来确定，而不用移除石笋，从而有助于减少科学取样对洞穴环境的影响。

**ABSTRACT**: Previous studies have analyzed the age distributions of stalagmites harvested from multiple caves and inferred important palaeoclimate changes that explain stalagmite growth phases. However, stalagmites may grow over tens of thousands of years; thus, they are irreplaceable. The value of speleothems to science must be weighed against their potential and current aesthetic and cultural value. In this study, we show that some palaeoclimate information can be extracted from a cave system without the removal of stalagmites. Our case study is based on basal U-Th dates for 77

individual stalagmites from thirteen caves located in and around Bantimurung-Bulusaraung National Park, southwest Sulawesi, Indonesia. The stalagmites grew during discrete intervals within the last ~530,000 years, and an analysis of their age distribution shows a first-order exponential decrease in the number of older stalagmites surviving to the present day. Further, this exponential relationship is observed in stalagmite populations around the world and is therefore likely to be a general cave phenomenon. Superimposed on the first-order exponential age distribution in southwest Sulawesi are positive anomalies in stalagmite growth frequency at 425–400, 385–370, 345-335, 330–315,160–155, 75–70 and 10–5 ka, which are typically coincident with wet periods on Borneo. To explain this distribution, we present a simple model of stalagmite growth and attrition. A first-order trend is controlled by processes intrinsic to karst systems that govern the natural attrition of stalagmites. These processes are nearly constant over time and result in the observed exponential relationship of stalagmite basal ages. Second-order variation is controlled by changes in the rate of stalagmite generation caused by fluctuating climates, which is a well-known concept in the speleothem literature. Removal of the exponential baseline allows for better assessment of relative peak heights and basic palaeoclimate information to be inferred. Importantly, the first- and second-order growth frequency variations can be characterized using basal stalagmite ages only, without the removal of stalagmites, thereby helping reduce the impact of scientific sampling on the cave environment.

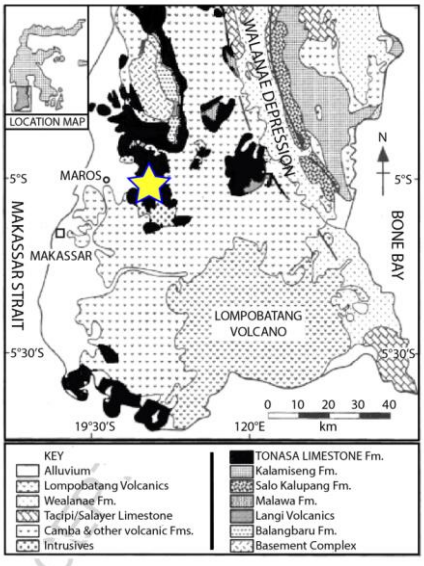


Figure 1. Geological map of southwest Sulawesi highlighting the Tonasa Limestone Formation (black) with the cave sites in the Maros region (yellow star). Adapted from Wilsonand Bosence (1996)

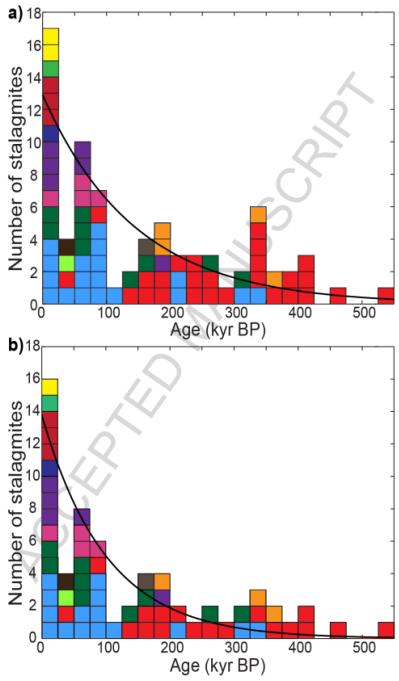


Figure 2. Distribution of mean stalagmite ages over the last ~530 kyr in 13 caves in southwest Sulawesi. a) Ages of all 77 stalagmites that were sampled. b) Ages of the adjusted set of 63 stalagmites after accounting for potential duplication of single drip-sites. Each individual cave is represented by a different color. Black curves show that a best-fit exponential relationship works as well for histogram data as it does for the probability density functions used elsewhere in this study.

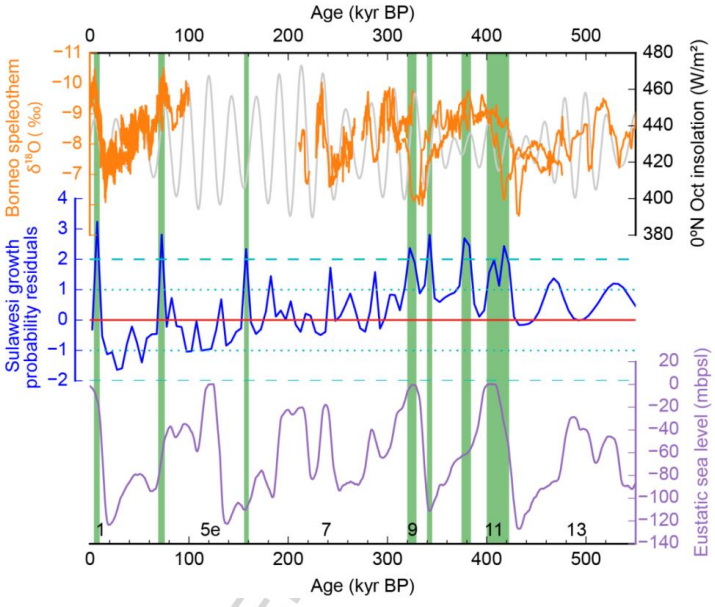


Figure 3. Comparison of stalagmite growth in Sulawesi with speleothem $\delta^{18}O$ records for Borneo and eustatic sea level. The distribution of stalagmite growth probability residuals (blue) for 13 caves in southwest Sulawesi compared with Borneo $\delta^{18}O$ records (orange; Partin et al., 2007, Meckler et al., 2012; Carolin et al., 2013) and 0°N October insolation (grey). Eustatic sea level (purple) is shown for reference (Bintanja and van de Wal, 2008), Interglacial marine isotope stages are numbered at the base. Green bars link >2σ peaks in Sulawesi stalagmite growth.

## 5. 甲烷、季风与千年尺度气候变化调控因素

翻译人：仲义 zhongy@sustech.edu.cn

*Kaustubh Thirumalai, Steven C. Clemens, and Judson W. Partin.* ***Methane, Monsoons, and Modulation of Millennial-Scale Climate*** *[J]. Geophysical Research Letters, 2020,47(9): e2020GL087613.*

**摘要：**地球轨道几何学特征通过调节太阳辐射变化对全球气候产生深远的影响。而在更新世的记录中，叠加在轨道周期变化之上，还存在以突变和快速变化为特征的千年尺度的巨大变化。然而，轨道强迫作用对于千年尺度变化的幅度和时间的调控影响程度还不得而知。本文作者从两个具有较好年代且具有岁差周期的记录（指示亚洲季风强度的石笋和大气甲烷）中分离出千年尺度变化幅度（MMV）。从千年尺度（1000-10000 年）记录来看，作者发现一个解耦特征，其中岁差直接驱动大气甲烷的千年变化而不是石笋氧同位素，这也与南极冰心 2H 的千年尺度变化一致。作者认为甲烷的千年尺度变化受控于中纬-高纬度日射量控制，而石笋氧同位素受控于内部气候反馈机制。

**ABSTRACT:** Earth's orbital geometry exerts a profound influence on climate by regulating changes inincoming solar radiation. Superimposed on orbitally paced climate change, Pleistocene records reveal substantial millennial-scale variability characterized by abrupt changes and rapid swings. However, the extent to which orbital forcing modulates the amplitude and timing of these millennial variations is unclear. Here we isolate the magnitude of millennial-scale variability (MMV) in two well-dated records, both linked to precession cycles (19,000- and 23,000-year periodicity): composite Chinese speleothem $\delta^{18}O$, commonly interpreted as a proxy for Asian monsoon intensity, and atmospheric methane. At the millennial timescale (1,000–10,000 years), we find a fundamental decoupling wherein precession directly modulates the MMV of methane but not that of speleothem $\delta^{18}O$, which is shown to be strikingly similar to the MMV of Antarctic ice core $\delta^{2}H$. One explanation is that the MMV of methane responds to changes in midlatitude to high-latitude insolation, whereas speleothem $\delta^{18}O$ is modulated by internal climate feedbacks.

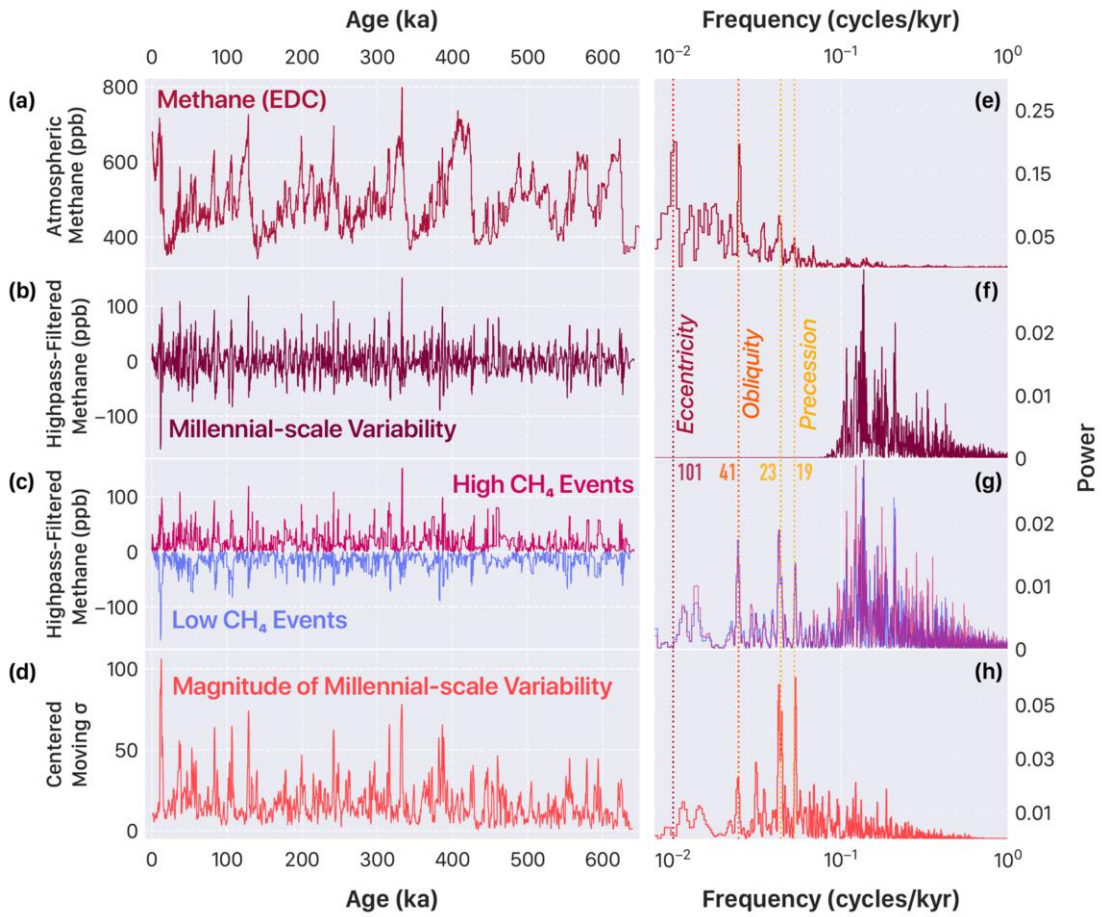


Figure 1. Orbital and millennial-scale atmospheric methane variability over the past 640 kyr. (a) EPICA Dome C record of $CH_4$, (b) its millennial-scale variability calculated as the 10-kyr high-pass filtered record of the original time series, (c) high-value and low-value $CH_4$ in the high-pass filtered record, and (d) the magnitude of millennial-scale variability (MMV) calculated as the centered rolling standard deviation of the high-pass filtered record using 2-kyr sliding windows (100-year step). (e–h) Periodograms of corresponding time series using the Lomb-Scargle methodology. Primary orbital frequencies are marked with dashed lines (19 and 23—precession; 41—obliquity; 101—eccentricity). Note different scaling for power spectral density. Strong peaks in the precessional band in the low-$CH_4$, high-$CH_4$, and MMV record indicate that insolation modulates the amplitude of millennial variations in atmospheric methane.

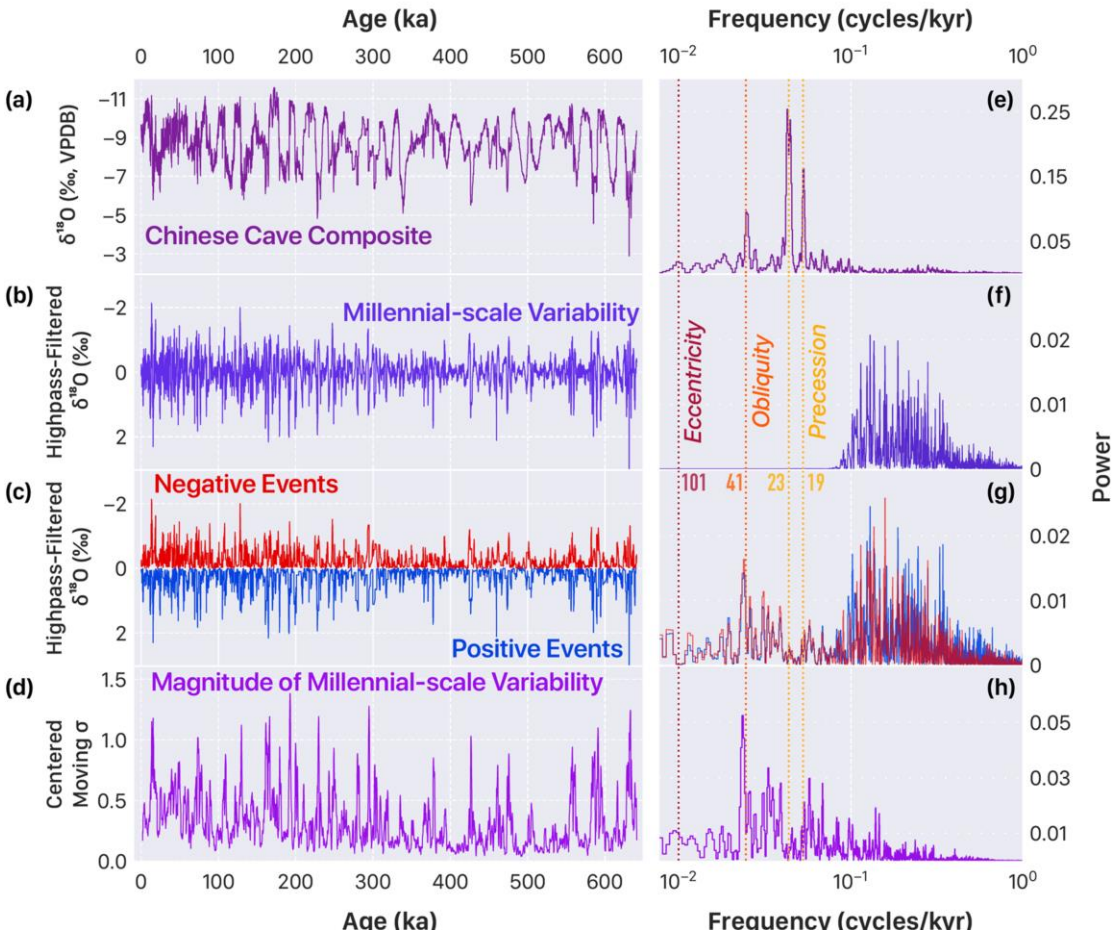


Figure 2. Orbital and millennial-scale variability in the composite Chinese speleothem record over the past 640 kyr. (a) Composite Chinese speleothem $\delta^{18}O$, (b) its millennial-scale variability calculated as the 10-kyr high-pass filtered record of the original time series, (c) negative-value and positive-value $\delta^{18}O$ in the high-pass filtered record, and (d) the magnitude of millennial-scale variability calculated as the centered rolling standard deviation of the high-pass filtered record using 2-kyr sliding windows (100-year step). (e–h) Periodograms of corresponding time series using the Lomb-Scargle methodology. Primary orbital frequencies are marked with dashed lines (19 and 23—precession; 41—obliquity; 101—eccentricity). Note different scaling for power spectral density. Despite that the "raw" $\delta^{18}O$ record contains strong concentrations of variance in the precessional band, the lack of peaks in the negative and positive events as well as in the MMV record suggest that precession does not modulate the envelope of millenial-scale $\delta^{18}O$ variations in the composite Chinese speleothem record.

## 6. 阿联酋蛇绿岩构造的地球物理成像

**翻译人：曹伟 11930854@mail.sustech.edu.cn**

*Ali, M.Y., Watts, A.B., Searle, M.P. et al.* ***Geophysical imaging of ophiolite structure in the United Arab Emirates.*** *Nat Commun 11, 2671 (2020). https://doi.org/10.1038/s41467-020-16521-0*

**摘要**：阿曼-阿联酋蛇绿岩被广泛应用于记录洋壳形成的地质过程。然而，蛇绿岩的几何结构，向阿曼湾的延伸以及深部地壳结构都有待探索。在本文中我们展示出蛇绿岩形成了一个高速、高密度、厚度大于 15Km 的向东倾斜岩体，在侵位过程中使之前的大陆边缘裂谷向下弯曲，从而导致了侧翼沉积盆地的沉降。蛇绿岩的西部陆上边界由 Semail 冲断层确定，而东界延伸至海上数公里，在地震剖面上由约 40°-45°的东倾正断层确定。该断层被解释为早期缝合带的西南边缘，缝合带将阿拉伯板块与现阶段沿马克兰海沟向北俯冲在欧亚板块之下的阿曼湾大洋地壳和地幔分开。

**ABSTRACT**：The Oman-United Arab Emirates ophiolite has been used extensively to document the geological processes that form oceanic crust. The geometry of the ophiolite, its extension into the Gulf of Oman, and the nature of the crust that underlies it are, however, unknown. Here, we show the ophiolite forms a high velocity, high density, >15 km thick east-dipping body that during emplacement flexed down a previously rifted continental margin thereby contributing to subsidence of flanking sedimentary basins. The western limit of the ophiolite is defined onshore by the Semail thrust while the eastern limit extends several km offshore, where it is defined seismically by a ~40–45°, east-dipping, normal fault. The fault is interpreted as the southwestern margin of an incipient suture zone that separates the Arabian plate from in situ Gulf of Oman oceanic crust and mantle presently subducting northwards beneath the Eurasian plate along the Makran trench.

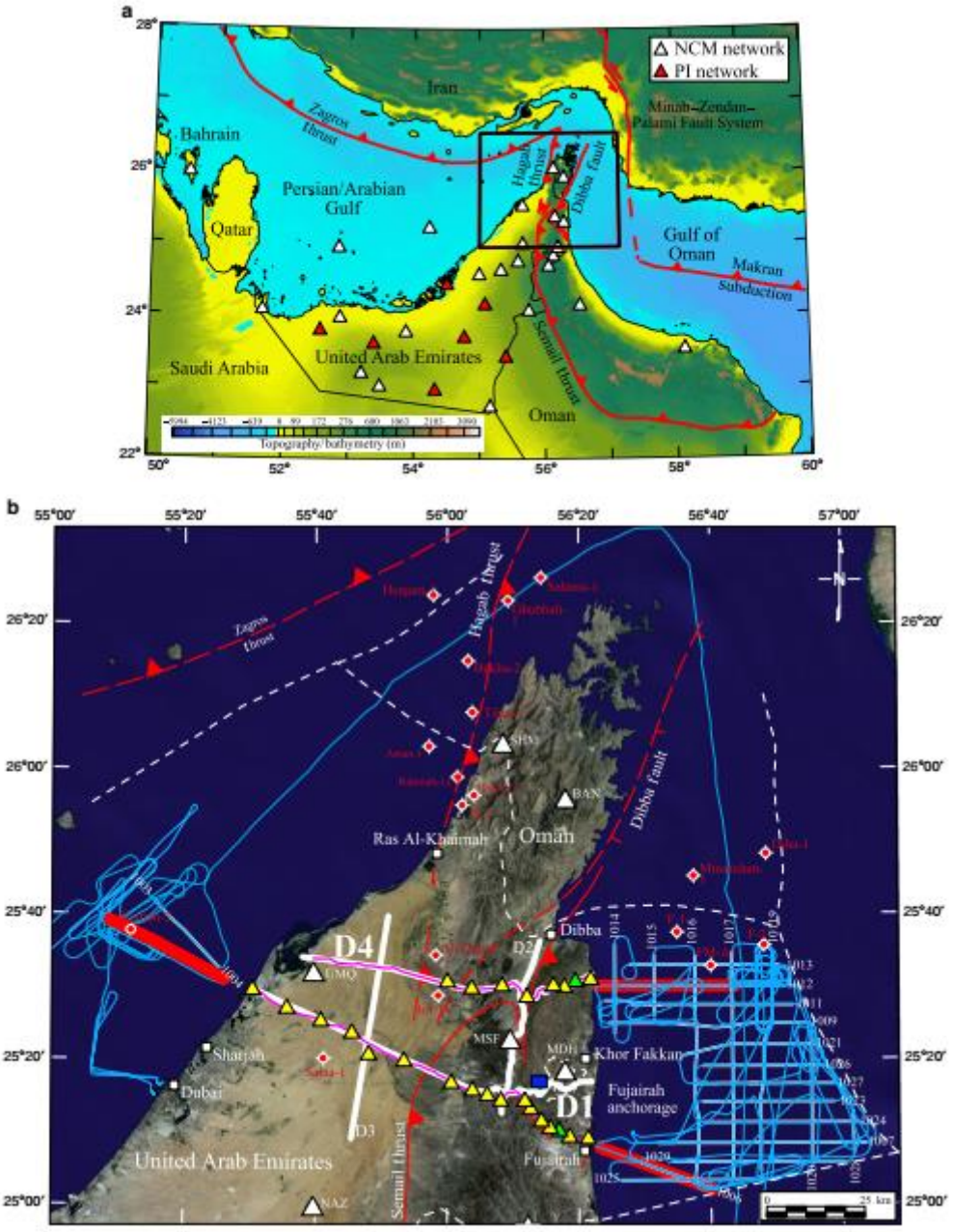


Figure 1. Location map showing the transects along which geological and geophysical data were acquired. a Study area (black box) and permanent passive seismic stations (white and red filled triangles).

b Landsat 9 image (https://www.geosoft.com/products/dap-server/overview) with geophysical data. Offshore: thick white lines = seismic reflection profiles; thin blue lines = gravity and magnetic anomaly data. Onshore: thick white lines = vibroseis seismic reflection profiles. Thin purple lines = gravity and magnetic anomaly data. Yellow filled triangles = Petroleum Institute (PI) seismic broadband stations. White filled triangles = National Centre of Meteorology (NCM) stations. Green filled triangles = Stations S-15 (D1) and S-19 (D4). Blue filled square locate the Bani Hamid granulites. Thin solid red lines delineate the Late Cretaceous Semail thrust and the Oligocene-early Miocene Hagab thrust and the Dibba fault. Dashed where uncertain. Figures constructed using Oasis Montaj.

## 7. 中晚全新世地中海气候变化：用小波分析研究西北地中海盆多代用指标多序列对比的贡献

翻译人：郑威 11930589@mail.sustech.edu.cn

Julien A, Pierre S, Vincent L, et al. ***Mid-to Late-Holocene Mediterranean climate variability: Contribution of multi-proxy and multi-sequence comparison using wavelet analysis in the northwestern Mediterranean basin***[J]. ***Earth-Science Reviews***, 2020: 103232.

**摘要：**全新世气候变化的驱动因素和机制依然没有被充分了解。这个工作讨论了已发表的古气候时间序列并且使用频谱分析来研究它们。这个方法可能可以突出不同信号间的共同特性并且使我们对气候变化的原因有更接近的理解。文章提出了使用小波分析对不均匀采样的时间序列进行频率成分对比的方法。文章最终得出结论：百年尺度太阳活动变化可能导致了类似于NAO的大气环流变化，从而影响西欧和地中海地区的风暴。狮子湾和大西洋的气候代用指标可能记录了热带循环周期，这可能突出了ENSO变化对地中海西部的影响。

**ABSTRACT：** Forcings and mechanisms underlying Holocene climate variability still remain poorly. This work review already published paleoclimatic time series and proposes an alternative way to compare them using spectral analysis. Such an approach may emphasize joint features between different signals and lead us closer to the causes of climate changes.

Ten paleoclimatic proxy records from 5 sequences from the Gulf of Lions and surrounding areas were compiled. These paleoclimate time-series were supplemented with proxies of the North Atlantic Oscillations (NAO), El Niño–Southern Oscillations (ENSO) and the Intertropical Convergence Zone (ITCZ) variability. A comparison of their frequency content is proposed using wavelet analysis for unevenly sampled time series. A new algorithm is used in order to propagate the age model errors within wavelet power spectra.

Three main groups of shared features specific to the Mid- and Late Holocene (after 7000 yrs cal BP) can be defined on the basis of the results of these analyses, an Atlantic cyclic period, solar cyclic periods and tropical cyclic periods. The Atlantic cyclic period is probably related to fluctuations of the Atlantic thermohaline circulation which would induce changes in the storm track extension and position thereby impacting upon precipitation and storminess over a millennial scale. The centennial

scale solar variability might induce a NAO-like variability of the atmospheric circulation thereby influencing storminess in Western Europe and Mediterranean. Finally, tropical cyclic periods are possibly registered in of the Gulf of Lions and Atlantic climate proxies, potentially highlighting the influence of ENSO variability over the western Mediterranean.

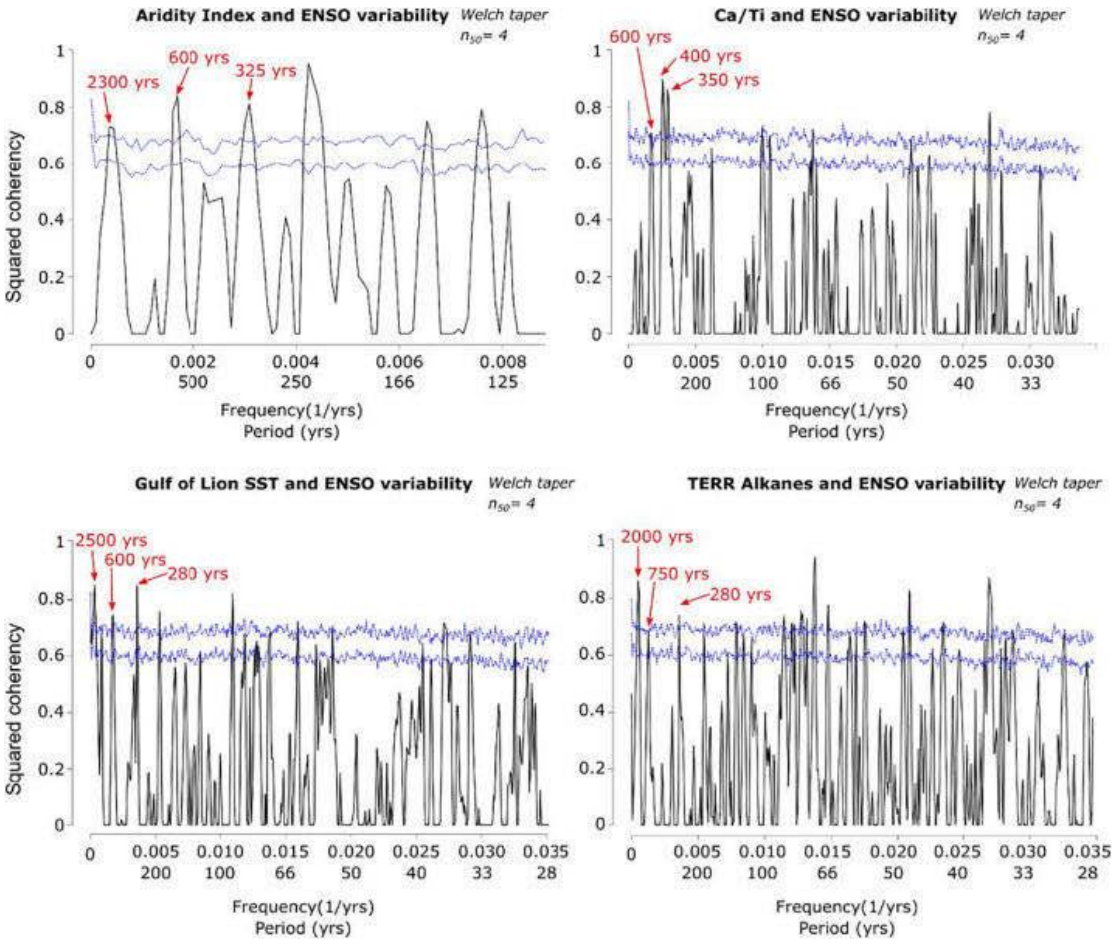


Figure 1. Comparison of the Sunspot number, the NAO indexes and the Palavas Storm Index (SI) filtered with a 150-300 yrs bandpass filter to highlight variations linked to the De Vries cycles. The filled red curves correspond to the variability within the bandwidth 150-300 yrs obtained by summing the wavelet power over several scales. The shaded blue boxes highlight time intervals characterized by concomitant high solar and NAO index variability within the bandwidth 150-300 yrs. The shaded orange box highlights a time interval characterized by concomitant high solar and storminess variability without NAO index variability within the bandwidth 150-300 yrs.

## 8. 南海北部边缘裂后期岩浆作用

**翻译人：刘伟 inewway@163.com**

*Qiliang Sun，Tiago M. Alves Minghui Zhao et al.* ***Post-rift magmatism on the northern South China Sea margin*** *[J].* ***GSA Bulletin, 2020****, https://doi.org/10.1130/B35471.1.*

**摘要：**高分辨率三维地震数据探测到了南海北部裂谷序列上的以广泛的火山和熔岩流形式存在的强烈岩浆活动。这种岩浆作用比海底扩张结束的时间晚了至少 6.8Ma。一条拆离断裂延伸至深部岩浆房，是岩浆在深部垂直运移的主要路径。而正断层和岩墙构成了一个浅部的运移系统，岩浆通过该系统从拆离断层运移并挤压到古海底。研究区火山活动发生时间约为 8.2 Ma ~1.1 Ma，并存在 5.2 Ma 和 2.8 Ma 两个峰值，与东沙运动相关。喷出的岩浆形成了火山和广阔的熔岩流；后者局限于沉积物波的槽中或沿着海底峡谷流动。总得来看，本研究表明：（1）年轻岩浆活动广泛分布于南海北部大陆边缘；（2）海底形态对深海火山的分布结构有较大影响；（3）区域构造活动的同裂谷断裂(特别是拆离断裂)密切控制着岩浆运移系统。

**ABSTRACT:** Intense magmatism in the form of widespread volcanoes and lava flows is identified in high-resolution 3-D seismic data over a post-rift sequence of the northern South China Sea (SCS). Such a magmatism post-dates the end of seafloor spreading in the SCS by at least 6.8 m.y. A detachment (boundary) fault propagating into a deep-seated magma chamber provided the main vertical pathway for magma migration. In turn, normal faults and dykes constituted a shallow plumbing system through which the magma migrated from the boundary fault and was extruded onto the paleo-seafloor. Volcanism occurred in the study area from ca. 8.2 Ma to ca. 1.1 Ma in the form of two distinct events, dated ca. 5.2 Ma and ca. 2.8 Ma, which are correlated with the Dongsha Event. Extrusive magma formed volcano edifices and extensive lava flows; the latter of which were confined to the troughs of sediment waves or, instead, flowed along submarine canyons. As a corollary, this study shows that in the SCS: (1) young magmatism is widespread on the northern continental margin, (2) seafloor morphology greatly influences the architecture of deep-water volcanoes, and (3) syn-rift faults (especially detachment faults) reactivated by regional tectonics closely control the magma plumbing systems.

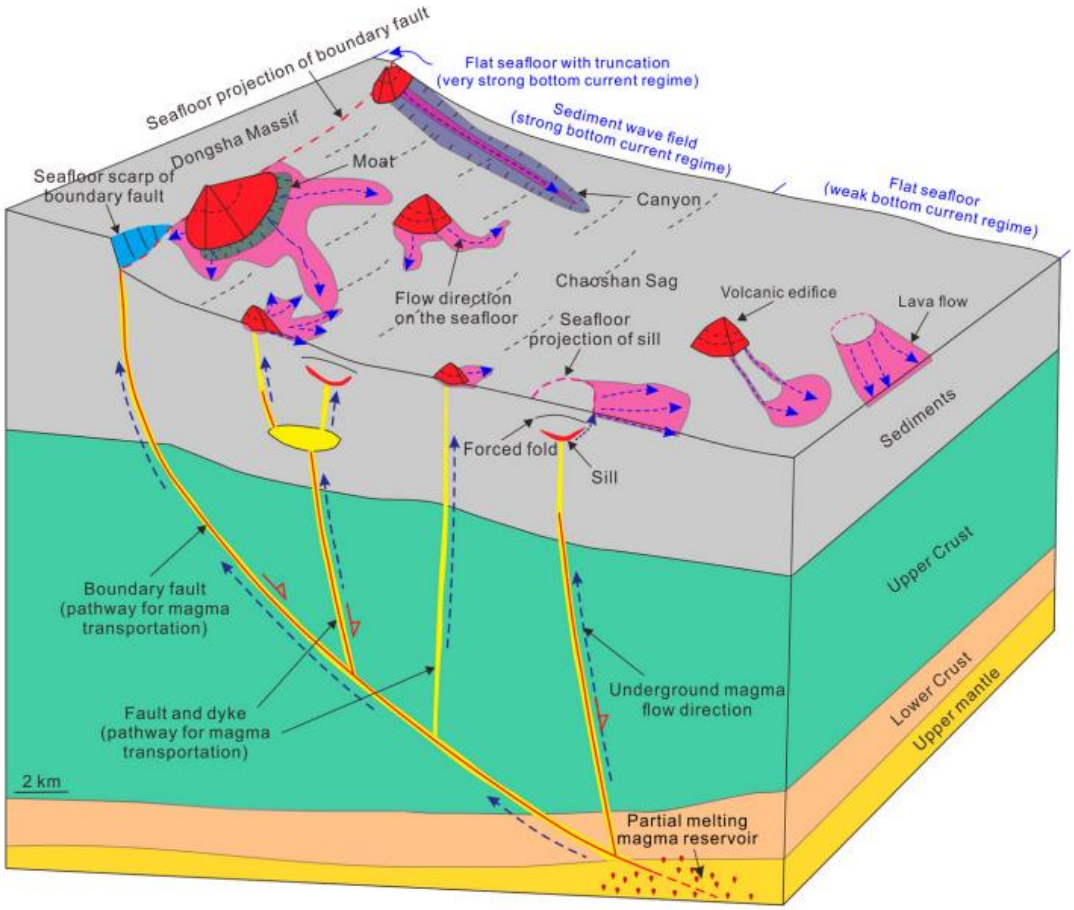


Figure 1. Model of the magma pluming system interpreted in the study area of the northern South China Sea. The magma sources from the partial melting reservoir and boundary fault serves as the main conduit for the upward migration of the magma. Secondary faults and dykes connecting with the boundary fault also provide vertical pathways for magma migration. The shallowly emplaced sills also feed the lava flows on the paleo-seafloor. Nearly all of the magma plumbing system is located in the hanging-wall block. The distribution of lava flows on the paleo-seafloor is mainly controlled by canyons and sediment waves (on an uneven seafloor) in the upper part of the hanging-wall, and controlled by the dip direction of paleo-seafloor in the lower part of the hanging-wall.